



Virginia Commonwealth University  
VCU Scholars Compass

---

Chemistry Publications

Dept. of Chemistry

---

2020

## Dissociation of Singly and Multiply Charged Nitromethane Cations: Femtosecond Laser Mass Spectrometry and Theoretical Modeling

G. L. Gutsev  
*Florida A&M University*

S. L. McPherson  
*Virginia Commonwealth University*

Hugo A. López Peña  
*Virginia Commonwealth University*

*See next page for additional authors*

Follow this and additional works at: [https://scholarscompass.vcu.edu/chem\\_pubs](https://scholarscompass.vcu.edu/chem_pubs)

 Part of the [Chemistry Commons](#)

2020 American Chemical Society

---

Downloaded from

[https://scholarscompass.vcu.edu/chem\\_pubs/110](https://scholarscompass.vcu.edu/chem_pubs/110)

This Article is brought to you for free and open access by the Dept. of Chemistry at VCU Scholars Compass. It has been accepted for inclusion in Chemistry Publications by an authorized administrator of VCU Scholars Compass. For more information, please contact [libcompass@vcu.edu](mailto:libcompass@vcu.edu).

---

**Authors**

G. L. Gutsev, S. L. McPherson, Hugo A. López Peña, Derrick Ampadu Boateng, L. G. Gutsev, B. R. Ramachandran, and Katharine M. Tibbetts

# Dissociation of Singly and Multiply Charged Nitromethane Cations: Femtosecond Laser Mass Spectrometry and Theoretical Modeling

Gennady L. Gutsev,<sup>\*,†</sup> Shane McPherson,<sup>‡</sup> Hugo A. López Peña,<sup>‡</sup> Derrick Ampadu Boateng,<sup>‡</sup> Lavrenty G. Gutsev,<sup>¶,§</sup> B. Ramu Ramachandran,<sup>¶</sup> and Katharine Moore Tibbetts<sup>\*,‡</sup>

<sup>†</sup>*Department of Physics, Florida A&M University, Tallahassee, Florida 32307, United States*

<sup>‡</sup>*Department of Chemistry, Virginia Commonwealth University, Richmond, Virginia 23284, United States*

<sup>¶</sup>*Institute for Micromanufacturing, Louisiana Tech University, Ruston, Louisiana 71272, United States*

<sup>§</sup>*Institute of Problems of Chemical Physics of Russian Academy of Sciences, Chernogolovka, Moscow District 142432, Russia*

E-mail: [gennady.gutsev@fam.u.edu](mailto:gennady.gutsev@fam.u.edu); [kmtibbetts@vcu.edu](mailto:kmtibbetts@vcu.edu)

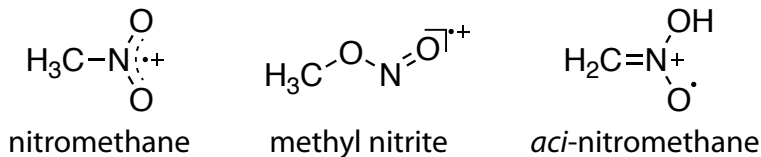
## Abstract

Dissociation pathways of singly- and multiply-charged gas-phase nitromethane cations were investigated with strong-field laser photoionization mass spectrometry and density functional theory computations. There are multiple isomers of the singly charged nitromethane radical cation, several of which can be accessed by rearrangement of the parent  $\text{CH}_3\text{-NO}_2$  structure with low energy barriers. While direct cleavage of the C–N

bond from the parent nitromethane cation produces  $\text{NO}_2^+$  and  $\text{CH}_3^+$ , rearrangement prior to dissociation accounts for fragmentation products including  $\text{NO}^+$ ,  $\text{CH}_2\text{OH}^+$ , and  $\text{CH}_2\text{NO}^+$ . Extensive Coulomb explosion in fragment ions observed at high laser intensity indicates that rapid dissociation of multiply charged nitromethane cations produces additional species such as  $\text{CH}_2^+$ ,  $\text{H}^+$ , and  $\text{NO}_2^{2+}$ . Based on analysis of Coulomb explosion in the mass spectral signals and pathway calculations, sufficiently intense laser fields can remove four or more electrons from nitromethane.

## 1 Introduction

The chemical reactions of nitromethane (NM) have been widely investigated for decades due to its importance to atmospheric chemistry<sup>1</sup> and use in propellants<sup>2</sup> and explosives.<sup>3</sup> As a model for nitrohydrocarbon energetic materials, understanding decomposition pathways of NM under extreme conditions is crucial for evaluating energetic material sensitivity, performance, and safety.<sup>4,5</sup> Shock detonation in NM is known to be initiated by the *aci*-anion ( $\text{CH}_2\text{NO}_2^-$ ) and protonated cation ( $\text{CH}_3\text{NO}_2\text{H}^+$ ) that are present in high quantities with added sensitizers<sup>6,7</sup> or under high pressure.<sup>8</sup> Moreover, shock conditions produce high ionic temperatures with electron densities exceeding  $\sim 10^{21} \text{ cm}^{-3}$ .<sup>9,10</sup> Hence, in addition to the widely studied reactions of neutral NM,<sup>5,11,12</sup> the decomposition pathways of NM ions are important for evaluating its behavior as an energetic material.



Scheme 1: Isomers of NM radical cation.

The dissociation reactions of isolated NM radical cation have been studied for decades with mass spectrometry.<sup>13-25</sup> Since the 1980's, NM radical cation has been known to exist in three isomeric forms shown in Scheme 1,<sup>17-20</sup> with both the methylnitrite and *aci*-

nitromethane structures accessible from the ionized parent nitromethane structure.<sup>21</sup> Both the methylnitrite and *aci*-nitromethane cation states are lower in energy than the parent NM cation state.<sup>18,19</sup>

The three isomers undergo distinct dissociation pathways. The nitromethane structure undergoes direct C–N bond cleavage to form  $\text{NO}_2^+$  or  $\text{CH}_3^+$ , and N–O cleavage from this structure produces  $\text{CH}_3\text{NO}^+$ .<sup>15</sup> The methylnitrite structure undergoes N–O bond cleavage to form  $\text{NO}^+$ <sup>15–18</sup> or  $\text{CH}_3\text{O}^+$  (observed as  $\text{CH}_2\text{OH}^+$ ).<sup>16,18</sup> The *aci*-nitromethane structure undergoes H loss to form  $\text{CH}_2\text{NO}_2^+$  and OH loss to form  $\text{CH}_2\text{NO}^+$ .<sup>19,21</sup> While extensive measurements on prepared methylnitrite,<sup>16–18</sup> *aci*-nitromethane,<sup>19–21</sup> and isotopically labeled species<sup>15,19</sup> have enabled these detailed pathway assignments, little quantum chemical modeling of NM cation decomposition has been performed.<sup>26,27</sup> Hence, many questions regarding the dissociation pathways of NM cation remain unanswered. New quantum chemical calculations are needed to enhance our understanding of the many possible dissociation pathways in NM radical cation, including those involving rearrangement to methylnitrite or *aci*-nitromethane structures.

In addition to radical cations, extreme conditions with high ionic temperatures and carrier densities may produce multiply charged cations.<sup>9,10</sup> The potential contributions of dications of the explosives 1,1-diamino-2,2-dinitroethene (FOX-7) and triaminotrinitrobenzene (TATB) to their ballistic properties have recently been investigated with density functional theory (DFT) simulations.<sup>28,29</sup> A recent investigation of the explosive trinitrotoluene (TNT) exposed to intense femtosecond laser pulses found evidence of multiply charged TNT cation formation based on observed Coulomb explosion that forms  $\text{NO}^+$  and  $\text{NO}_2^+$  fragments.<sup>30</sup> More broadly, multiply charged organic cations are of interest because they challenge traditional notions of chemical bonding,<sup>31</sup> contribute to chemical reactions in the interstellar medium<sup>32</sup> and ionosphere,<sup>33</sup> and can play a role in biological radiation damage.<sup>34</sup> However, to the best of our knowledge multiply charged cations in NM have neither been observed experimentally nor studied computationally.

Recently, we have reported on dissociation reactions in the radical cations of dimethyl methylphosphonate (DMMP),<sup>35,36</sup> nitrotoluene isomers,<sup>37,38</sup> and aniline<sup>39</sup> using femtosecond (fs) laser mass spectrometry and high level quantum chemical calculations. Evidence of multiply charged cations in DMMP and nitrotoluene isomers came from observed Coulomb explosion of fragment ion signals,<sup>35,37</sup> while the intact aniline dication and trication were directly observed.<sup>39</sup> In this work, we report mass spectra of NM that indicate formation of previously unreported fragments including  $\text{NO}_2^{2+}$ ; identify new stable isomers of NM cation and dication; and determine dissociation pathways in the NM cation, dication, trication, and higher charge states through analysis of Coulomb explosion signals and dissociation pathway computations.

## 2 Methods

### 2.1 Experimental Section

The experimental setup has been described in detail in our previous work.<sup>35,39</sup> Briefly, the output of a commercial Ti:Sapphire regenerative amplifier (Astrella, Coherent, Inc.) producing 2 mJ, 30 fs pulses centered at 800 nm was directed into an optical parametric amplifier (OPA, TOPAS Prime). The OPA produced 1300 nm, 125  $\mu\text{J}$ , 20 fs pulses. The output beam was passed through a  $\lambda/2$  waveplate that was set to either  $0^\circ$  or  $45^\circ$  relative to the optical axis. The  $0^\circ$  and  $45^\circ$  orientations result in the laser polarization being parallel or perpendicular to the time-of-flight mass spectrometer (TOFMS) flight axis. The laser was focused into the extraction region of the TOFMS (base pressure  $2 \times 10^{-9}$  Torr) using a  $f = 20$  cm fused silica lens, reaching intensities in the range of  $4 \times 10^{13}$  to  $2.8 \times 10^{14}$   $\text{W cm}^{-2}$  based on previous calibration using  $\text{Xe}^{n+}$  ion signal. Nitromethane (99%, Sigma Aldrich) was introduced into the TOFMS and through a variable leak valve until it reached a pressure in the range of  $2.0 - 2.5 \times 10^{-7}$  Torr. Mass spectra were recorded by averaging the signal of  $10^5$  laser shots using a 1 GHz digital oscilloscope (LeCroy WaveRunner 610Zi).

## 2.2 Computational Section

Our computations were performed using density functional theory (DFT) with the hybrid long-range corrected  $\omega$ B97XD functional<sup>40</sup> as implemented in GAUSSIAN 16.<sup>41</sup> This approach was found to be the best among several others belonging to both DFT and post-HF groups of quantum chemistry methods in computations of 2-nitrotoluene, a congener of nitromethane.<sup>38</sup> We chose the aug-cc-PVTZ basis set<sup>42</sup> consisting of the  $(4s3p2d)$  subset for H and the  $(5s4p3d2f)$  subsets for C, N, and O.

The choice of the  $\omega$ B97XD/aug-cc-PVTZ level of theory was validated by comparison of the computed values of the proton affinity (PA) and adiabatic ionization energy ( $IE_{\text{ad}}$ ) of nitromethane with the experimental data from the NIST webbook.<sup>43</sup> The PA value was computed<sup>44</sup> according to the formula  $E_{\text{tot}}(\text{AH}^+) = E_{\text{tot}}(A) + \text{PA}$ , where  $E_{\text{tot}}$  is the sum of the electronic and the zero-point vibrational energies and  $A = \text{CH}_2\text{NO}_2$ . Adiabatic ionization energies ( $IE_{\text{ad}}$ ) of the neutral nitromethane, its cation, and dication were computed as the difference in total energies of the states (with geometrical structures shown in Figure 2 below) according to the formula

$$IE_{\text{ad}} = E_{\text{tot}}^{\text{El}}(\text{CH}_3\text{NO}_2^{k+}) + E_0(\text{CH}_3\text{NO}_2^{k+}) - \left[ E_{\text{tot}}^{\text{El}}(\text{CH}_3\text{NO}_2^{(k-1)+}) + E_0(\text{CH}_3\text{NO}_2^{(k-1)+}) \right] \quad (1)$$

where  $k = 0-2$ ,  $E_{\text{tot}}^{\text{el}}$  is the total electronic energy, and  $E_0$  is the zero-point vibrational energy calculated within the harmonic approximation. Since no geometrically stable state of the nitromethane tetracation was found, the trication  $IE_{\text{ad}}$  cannot be computed. The vertical ionization energy ( $IE_{\text{vert}}$ ) corresponds to the instantaneous electron detachment when the geometry of an ionized species has no time to relax. The  $IE_{\text{vert}}$  values are computed as the difference in the electronic energies

$$IE_{\text{vert}} = E_{\text{tot}}^{\text{El}}(\text{CH}_3\text{NO}_2^{k+}) - E_{\text{tot}}^{\text{El}}(\text{CH}_3\text{NO}_2^{(k-1)+}) \quad (2)$$

Our  $IE_{\text{ad}}$  and PA values for neutral NM of 11.03 eV and 747.5 kJ/mol, respectively, are in very good agreement with the corresponding experimental values of  $11.08 \pm 0.04$  eV and 754.6 kJ/mol.<sup>43</sup> Computed values of  $IE_{\text{vert}}$  and  $IE_{\text{ad}}$  for all charge states of NM are given in Table 1. It is notable that the  $IE_{\text{vert}}$  value of the dication is smaller than the adiabatic value, which reflects the metastable character of the dication state.

Table 1: Adiabatic and vertical ionization energies for NM and its cations.

species	$IE_{\text{ad}}$ (eV)	$IE_{\text{vert}}$ (eV)
$\text{CH}_3\text{NO}_2$	11.03	11.54
$\text{CH}_3\text{NO}_2^+$	19.99	19.92
$\text{CH}_3\text{NO}_2^{2+}$	26.44	28.58
$\text{CH}_3\text{NO}_2^{3+}$	...	36.69

The optimization of each state was performed first without symmetry constraints and was followed by the harmonic vibrational frequency calculations to confirm the stationary character of the optimized state. If a geometrical structure obtained possessed apparent symmetry (predominantly  $C_s$ ), the optimization was repeated within assumed symmetry constraints. The convergence threshold for total energy was set to  $10^{-8}$  eV and the force threshold was set to the default value of  $10^{-3}$  eV/Å. We performed an extensive search for various decay pathways of the nitromethane cation and dication. Charges on fragments obtained from these pathways were computed by summing the natural atomic orbital charges. Transition states were found by either using trial geometries with the optimization option “TS” and/or a relaxed potential energy scan. Each transition state found was used as an input for the internal reaction coordinate (IRC)<sup>45</sup> calculation. If the latter arrived at a state which does not match the final state from the preceding step, another TS was searched for and so on until the full continuous decay profile is found.

# 3 Results and Discussion

## 3.1 Overview

Figure 1 shows mass spectra of NM recorded at  $4 \times 10^{13}$ ,  $8 \times 10^{13}$ , and  $1.6 \times 10^{14}$  W cm<sup>-2</sup> (40, 80, and 160 TW cm<sup>-2</sup>). This intensity range encompasses both multiphoton and tunneling ionization regimes based on the Keldysh parameter,  $\gamma = \omega_0 \sqrt{2m_e(IE_{\text{vert}})}/eE_0$ , defined by the laser frequency  $\omega_0$ , electron mass  $m_e$ ,  $IE_{\text{vert}}$  of NM, electron charge  $e$ , and laser field strength  $E_0$ .<sup>46</sup> The value  $\gamma \sim 1$  at 40 TW cm<sup>-2</sup> corresponds to the transition from the multiphoton regime with  $\gamma \gg 1$  to tunneling regime with  $\gamma \ll 1$ . At higher intensities in our experiments, ionization is predominantly in the tunneling regime.

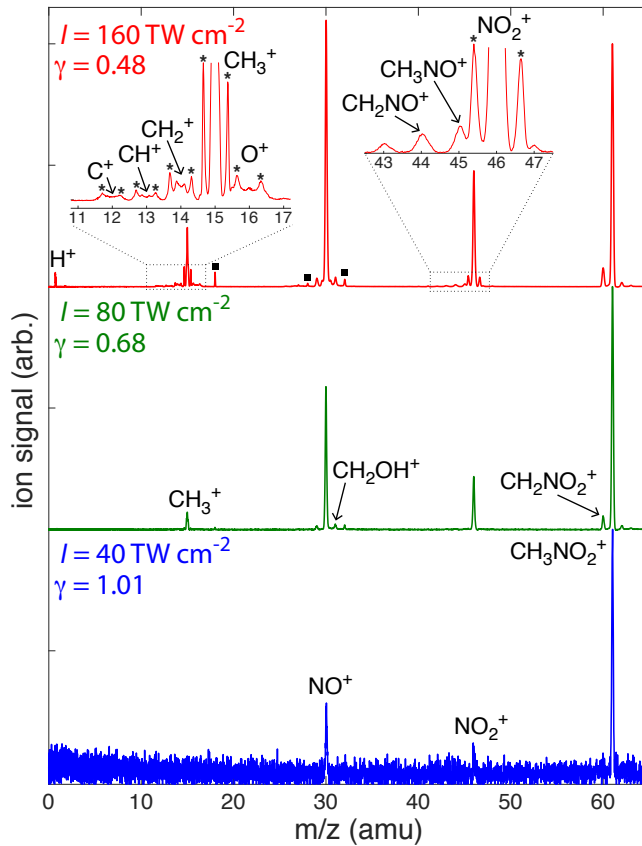


Figure 1: Mass spectra of NM taken at 40 (blue), 80 (green), and 160 (red) TW cm<sup>-2</sup> intensity. Selected fragments are labeled. Peaks indicated with \* arise from Coulomb explosion. Contaminants from air ( $\text{H}_2\text{O}^+$ ,  $\text{N}_2^+$ ,  $\text{O}_2^+$ ) are indicated by black squares.

In Figure 1, all signals are normalized to the yield of the parent molecular ion  $\text{CH}_3\text{NO}_2^+$

( $m/z$  61) signal. At 40 TW  $\text{cm}^{-2}$  (blue spectrum), slightly above the ionization threshold, the parent ion is the most intense peak, and small amounts of  $\text{NO}_2^+$  ( $m/z$  46) and  $\text{NO}^+$  ( $m/z$  30) are visible. At 80 TW  $\text{cm}^{-2}$  (green spectrum), the signals of  $\text{CH}_3^+$  ( $m/z$  15),  $\text{CH}_2\text{OH}^+$  ( $m/z$  31), and  $\text{CH}_2\text{NO}_2^+$  ( $m/z$  60) are also visible. At this intensity, the four most intense peaks are  $\text{CH}_3\text{NO}_2^+$ ,  $\text{NO}_2^+$ ,  $\text{NO}^+$ , and  $\text{CH}_3^+$ , consistent with previous fs laser ionization mass spectrometry measurements on NM.<sup>22–24</sup> At 160 TW  $\text{cm}^{-2}$ , two new features are visible. First, small yields of  $\text{CH}_3\text{NO}^+$ ,  $\text{CH}_2\text{NO}^+$ ,  $\text{CH}_n^+$  ( $n = 0 - 2$ ), and  $\text{H}^+$  are visible. Second, the  $\text{CH}_3^+$ ,  $\text{NO}_2^+$ ,  $\text{CH}_n^+$ , and  $\text{O}^+$  signals exhibit side peaks marked with a \*, indicating formation by Coulomb explosion of a multiply charged precursor. Coulomb explosion upon fs laser ionization has previously been observed in related molecules including aniline,<sup>39</sup> nitrotoluenes,<sup>30,37</sup> and TNT.<sup>30</sup>

Because the presence of Coulomb explosion peaks in our mass spectra indicates that multiply charged NM cations are formed by fs laser ionization, we first computed the energies of NM cations with the  $\text{CH}_3\text{-NO}_2$  topology of neutral NM, shown in Figure 2. Geometrically stable structures up to the trication  $\text{CH}_3\text{NO}_2^{3+}$  were found, whereas at higher charges no metastable states were observed: all optimizations of different trial geometries in the range of possible spin multiplicities led to the dissociative formation of several charged fragments. Independent of charge, the  $\text{CH}_3\text{-NO}_2$  topology does not represent the most stable isomer, as will be discussed in more detail below.

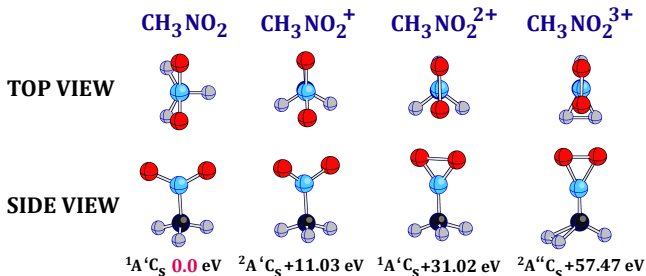


Figure 2: The optimized states of NM and its singly, doubly, and triply positively charged ions. All energies are given with respect to the total energy of the neutral NM state.

In Section 3.2, we report 25 geometrically stable isomers of  $\text{NM}^+$  and how some of

these isomers contribute to dissociation pathways producing the observed fragment ions in Figure 1. In Section 3.3, we elucidate dissociation pathways of multiply charged NM cations through analysis of the Coulomb explosion features and reaction pathway computations. The collective findings are discussed in Section 3.4.

## 3.2 Reaction pathways of singly charged nitromethane cation

We consider the reaction pathways of the NM cation leading to the fragments  $\text{NO}_2^+$ ,  $\text{CH}_3^+$ ,  $\text{CH}_3\text{NO}^+$ ,  $\text{NO}^+$ ,  $\text{CH}_2\text{OH}^+$ ,  $\text{CH}_2\text{NO}^+$ , and  $\text{CH}_2\text{NO}_2^+$ . The computed decay energies and threshold intensities at which each fragment appears are provided in the Supporting Information, Tables S1 and S2. We first consider direct dissociation of the  $\text{NM}^+$  cation with  $\text{CH}_3\text{-NO}_2$  topology (Section 3.2.1). Second, we determine rearrangement pathways of the  $\text{NM}^+$  cation into its more stable isomers (Section 3.2.2). Finally, we address the dissociation pathways of these rearranged  $\text{NM}^+$  cation isomers (Section 3.2.3).

### 3.2.1 Direct dissociation pathways from $\text{NM}^+$

Figure 3 shows the computed potential energy curves for direct dissociation of the  $\text{NM}^+$  structure. Cleavage of the C–N bond to produce  $\text{NO}_2^+$  and  $\text{CH}_3^+$  is shown in Figure 3a. The energy difference between producing  $\text{NO}_2^+$  (1.05 eV) and  $\text{CH}_3^+$  (1.18 eV) is only 0.13 eV (Supporting Information, Table S1), consistent with the similar ionization energy values of 9.60 eV and 9.84 eV for  $\text{NO}_2$  and  $\text{CH}_3$ , respectively.<sup>43</sup> Despite the expected similar appearance energies, no  $\text{CH}_3^+$  was detected at 40  $\text{TW cm}^{-2}$  in our mass spectra (c.f., Figure 1 and Table S2), consistent with previous mass spectrometry investigations that found that  $\text{CH}_3^+$  appears only at energies at least 1 eV above the appearance energy for  $\text{NO}_2^+$ .<sup>13,14,25</sup> According to our computations, a bifurcation point (BP) occurs at a C–N distance of 1.70 Å, where the charge on the  $\text{NO}_2$  and  $\text{CH}_3$  fragments are equal (+0.5e). At larger C–N distances, the charge migrates to the  $\text{NO}_2$  fragment, following the path shown in green diamonds. To illustrate the analogous path with the charge on the  $\text{CH}_3$  fragment, we plot a curve with red

dots that is higher than the lower energy curve by 0.13 eV at long C–N distances. Cleavage of the N–O bond to produce  $\text{CH}_3\text{NO}^+$  (Figure 3b) requires twice the energy (2.13 eV) compared to producing  $\text{NO}_2^+$ . This higher energy requirement is consistent with the  $\text{CH}_3\text{O}^+$  fragment only appearing in low quantities at intensities exceeding  $70 \text{ TW cm}^{-2}$  (Table S2).

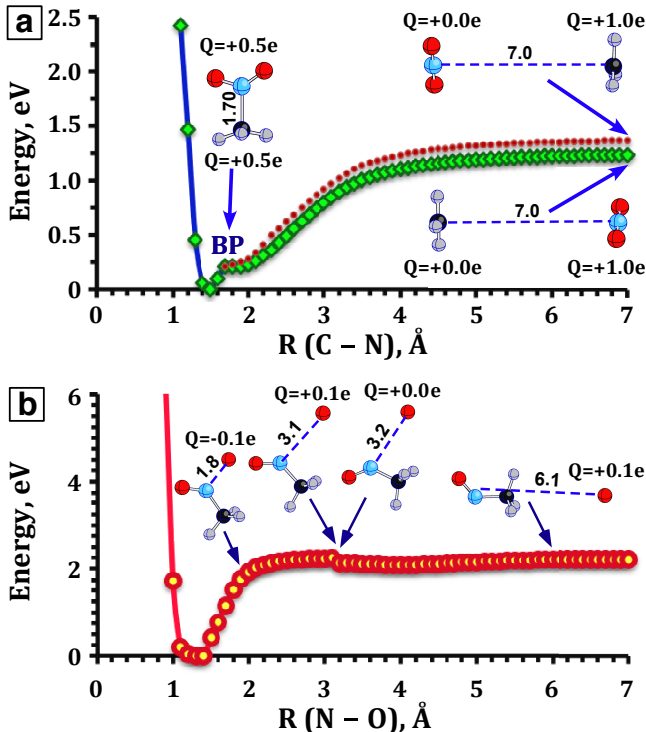


Figure 3: Potential energy curves corresponding to (a) the  $\text{CH}_3\text{--NO}_2$  bond stretch and (b) the  $\text{CH}_3\text{NO--O}$  bond stretch in  $\text{NM}^+$ . In (a), **BP** denotes the bifurcation point where the charges of the  $\text{CH}_3$  and  $\text{NO}_2$  units are equal ( $+0.5 e$ ). In (b), four structures at intermediate  $R(\text{N--O})$  values are shown. The kink in the curve arises when the O atom loses all charge at  $R(\text{N--O}) = 3.2 \text{ \AA}$ .

### 3.2.2 Rearrangements of nitromethane cation

Twenty-five geometrically stable isomers were found for  $\text{NM}^+$  (Figure 4), labeled **I–XXV** in order of increasing energy. The 11.03 eV energy for the nitromethane structure (**XXII**, blue box) is in good agreement with the experimentally reported  $IE_{\text{ad}}$  of  $11.08 \pm 0.04 \text{ eV}$ .<sup>43</sup> Although our energies for the *aci* isomers **XVI** and **XVII** (magenta box) of 9.95 and 10.23 eV are higher than the experimentally reported 9.4 eV, the latter thermochemical value

was obtained from decomposition of the 1-nitropropane cation and not direct ionization of *aci*-nitromethane.<sup>19</sup> Our energies of 10.26 and 10.42 eV for the *trans*- and *cis*-methylnitrite isomers **XVIII** and **XIX** (green box) closely match the experimentally reported 10.4 eV  $IE_{ad}$  for methylnitrite.<sup>17,18</sup> It is notable that isomer **III** has been proposed in a previous computational study as an intermediate in methylnitrite cation dissociation to produce  $CH_2OH^+$ .<sup>27</sup>

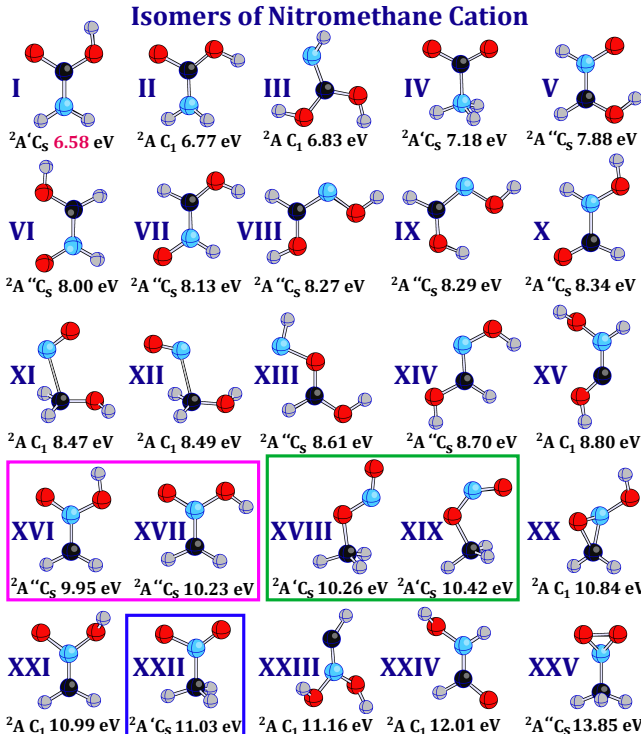


Figure 4: The optimized states of isomers of the nitromethane cation. All energies (in eV) are given with respect to the total energy of neutral NM. The blue, green, and magenta boxes denote the nitromethane, methylnitrite, and *aci*-nitromethane structures from Scheme 1

Rearrangement pathways from the  $NM^+$  isomer **XXII** leading to methylnitrite and *aci*-nitromethane structures are shown in Figure 5. In the nitro-nitrite rearrangement (NRR, Figure 5a)  $NM^+$  passes through a transition state (TS1) with 0.86 eV to reach the *trans*-methylnitrite (**XVIII**). The *trans*-methylnitrite can interconvert to the *cis*-methylnitrite (**XIX**) through a second transition state (TS2). *Aci*-rearrangement (Figure 5b) was found to convert the  $NM^+$  isomer (**XXII**) to four different *aci*-nitromethane structures (**XVI**, **XVII**, **XI**, and **V**), all of which can be reached spontaneously after overcoming the initial

barrier of 1.11 eV (TS1). While *aci*-nitromethane with the topology of isomers **XVI** and **XVII** has been reported via preparation from 1-nitropropane cation<sup>19,20</sup> and inferred from dissociation reactions of  $\text{NM}^+$ ,<sup>21</sup> our computations indicate that the lower-energy isomers **XI** and **V** may also be accessed directly from the  $\text{NM}^+$  structure.

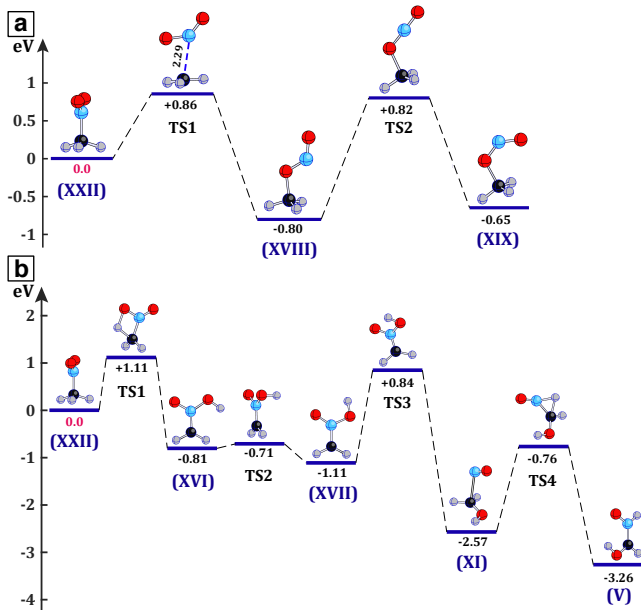


Figure 5: Rearrangements of  $\text{NM}^+$ : Nitro-nitrite rearrangement leading to methylnitrite structures (a); *Aci*-rearrangement leading to four *aci*-nitromethane isomers (b).

### 3.2.3 Dissociation of rearranged nitromethane cation structures

The potential energy curves showing dissociation pathways to produce  $\text{NO}^+$  and  $\text{CH}_2\text{OH}^+$  are shown in Figures 6a and 6b, respectively. The  $\text{NO}^+$  fragment is produced by cleavage of the O–N bond from the *trans*-methylnitrite structure **XVIII** (Figure 6a). The dissociation limit from the energy minimum of **XVIII** is 1.00 eV, but the final product corresponds to a  $\text{CH}_3\text{O}$  isomer 0.31 eV above the lowest energy isomer  $\text{CH}_2\text{OH}$ . Considering the  $\text{CH}_3\text{O} \rightarrow \text{CH}_2\text{OH}$  isomerization and the energy difference between isomers **XVIII** and **XXII** results in a decay energy of -0.07 eV relative to the  $IE_{\text{ad}}$  of  $\text{NM}$  (Table S1). The effective dissociation barrier is equal to the transition state energy of 0.86 eV leading to *trans*-methylnitrite from the initial  $\text{NM}^+$  (c.f., Figure 5a). This small dissociation barrier explains the reported appearance

energy of  $\text{NO}^+$  only  $\sim 0.7$  eV above the NM ionization threshold<sup>13,14,18,21</sup> and the appearance of  $\text{NO}^+$  at the lowest intensity of  $\sim 35$  TW  $\text{cm}^{-2}$  producing ion signal from NM in our experiments (Table S2). The  $\text{CH}_2\text{OH}^+$  fragment can be formed via cleavage of the C–N bond from the *aci* structure **XI**. The energy of isomer **XI** dissociation to  $\text{CH}_2\text{OH}^+$  and NO is 0.53 eV, which results in a decay energy of -2.01 eV relative to  $\text{NM}^+$ . However, the effective dissociation barrier is equal to the initial transition state energy of 1.11 eV leading to the first *aci*-rearrangement (c.f., Figure 5b). This higher effective barrier to produce  $\text{CH}_2\text{OH}^+$  as compared to  $\text{NO}^+$  is consistent with the significantly higher yield of  $\text{NO}^+$  compared to  $\text{CH}_2\text{OH}^+$  in our experiments and in previous literature on NM cation.<sup>13,15,18</sup>

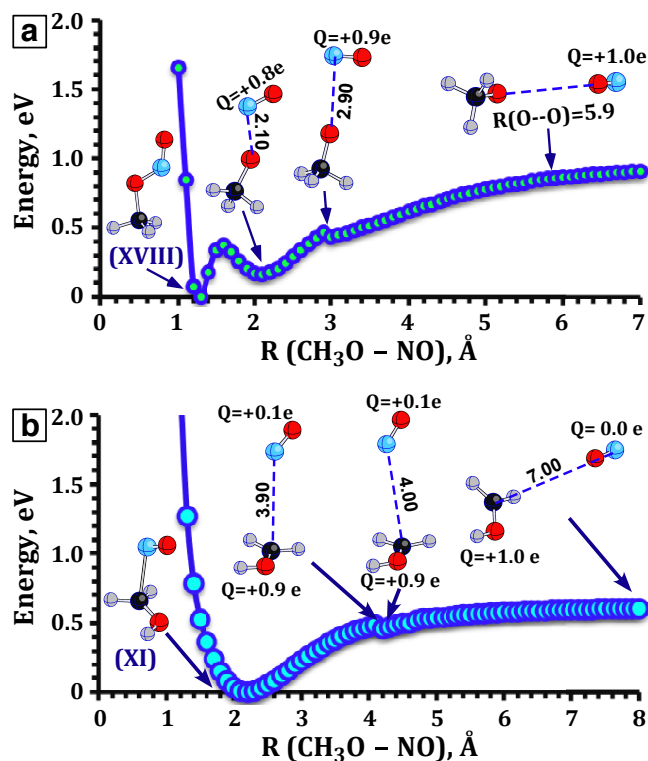


Figure 6: Potential energy curves corresponding to the  $\text{CH}_3\text{O}-\text{NO}$  stretch in (a) the methyl nitrite cation **XVIII** and (b) the *aci*-nitromethane cation **XI**. For both curves, three structures are shown at intermediate  $R(\text{CH}_3\text{O}-\text{NO})$  values with the charges of each fragment.

Two dissociation pathways producing  $\text{CH}_2\text{NO}^+$  were found: one from the conventional *aci*-isomer **XVI** (Figure 7a) and the second from the low-energy isomer **V** (Figure 7b). In both cases, the transition state energies required for OH loss are below the 1.11 eV required

for the initial *aci*-rearrangement (c.f., Figure 5b), so the effective dissociation barrier to form  $\text{CH}_2\text{NO}^+$  from  $\text{NM}^+$  is 1.11 eV. Despite this relatively low barrier, little  $\text{CH}_2\text{NO}^+$  signal is seen in our mass spectra (Figure 1). Nevertheless, the dissociation barriers below 1 eV from the *aci* structures explain the high yields of  $\text{CH}_2\text{NO}^+$  observed from collision-induced dissociation of  $\text{NM}^+$  and prepared *aci*-nitromethane cation.<sup>19</sup>

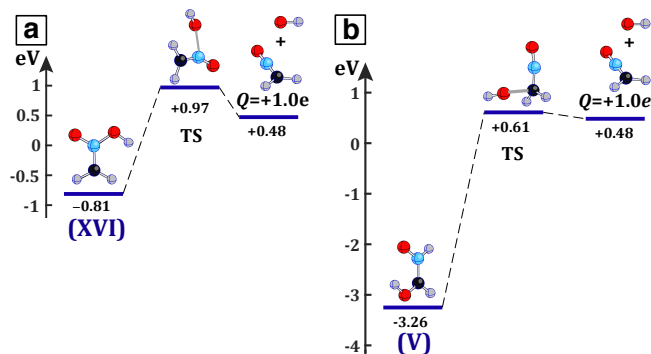


Figure 7: Pathways for OH loss from *aci* isomers **XVI** and **V**. Energies are with respect to the energy of  $\text{NM}^+$  isomer **XXII** at 0.0 eV.

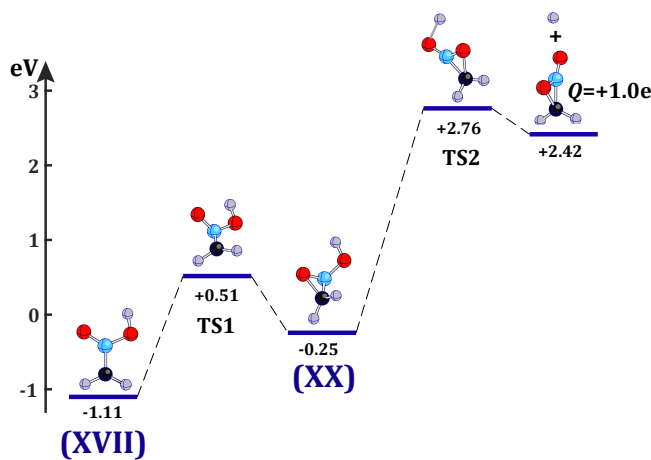


Figure 8: Pathway for H atom loss from *aci* isomer **XVII**. Energies are with respect to the energy of  $\text{NM}^+$  isomer **XXII** at 0.0 eV.

Hydrogen atom loss leading to the  $\text{CH}_2\text{NO}_2^+$  fragment was found to proceed from *aci* isomer **XVII** (Figure 8). The cyclic isomer **XX** is an intermediate reached via TS1, 0.51 eV above  $\text{NM}^+$ . Dissociation of isomer **XX** requires substantially more energy than the previous pathways considered, with the TS2 barrier of 2.76 eV and a decay energy of 2.42 eV above

NM<sup>+</sup>. Nevertheless, the H loss from the *aci*-nitromethane structure requires considerably less energy than the 4 eV required for direct H loss from NM<sup>+</sup> (Supporting Information, Figure S1). Hence, our results explain previous experimental observation of H loss from the *aci*-nitromethane structure during collision-induced dissociation of NM<sup>+</sup>.<sup>21</sup> It is notable that a higher yield of CH<sub>2</sub>NO<sub>2</sub><sup>+</sup> relative to both CH<sub>2</sub>OH<sup>+</sup> and CH<sub>2</sub>NO<sup>+</sup> is observed in our mass spectra (c.f., Figure 1) despite this pathway requiring more energy. Some of the CH<sub>2</sub>NO<sub>2</sub><sup>+</sup> could arise from dissociation of the NM dication, as discussed in Section 3.3.2 below.

### 3.3 Dissociation pathways of multiply charged nitromethane cations

In this section, we first identify fragment ions produced by Coulomb explosion and the specific dissociation pathway of NM dication to NO<sub>2</sub><sup>+</sup> and CH<sub>3</sub><sup>+</sup> based on analysis of the momentum and kinetic energy release from Coulomb explosion (Section 3.3.1). Second, we identify stable isomers of the NM dication and compute its dissociation pathways that produce NO<sub>2</sub><sup>+</sup> and CH<sub>3</sub><sup>+</sup>; and H<sup>+</sup> and CH<sub>2</sub>NO<sub>2</sub><sup>+</sup> (Section 3.3.2). Finally, we compute dissociation pathways of higher NM cation charge states that produce additional Coulomb explosion products NO<sub>2</sub><sup>2+</sup>, CH<sub>2</sub><sup>+</sup>, CH<sup>+</sup>, O<sup>+</sup>, H<sup>+</sup>, and H<sub>2</sub><sup>+</sup> (Section 3.3.3).

#### 3.3.1 Coulomb explosion analysis

To determine the timescale of Coulomb explosion from multiply charged NM cations, mass spectra were measured with the laser polarization both parallel and perpendicular to the time-of-flight axis. If dissociation occurs within a single rotational period, energetic fragments will be preferentially ejected along the laser polarization axis, while fragments will be ejected isotropically if dissociation occurs on longer timescales.<sup>47–50</sup> Hence, when dissociation is rapid, well-resolved Coulomb explosion peaks to the left and right of the nominal m/z peak will only be visible when the laser polarization is parallel to the TOF axis. In contrast, when the polarization is orthogonal, the anisotropically ejected fragments will arrive at the detector at the same time and produce only one peak.

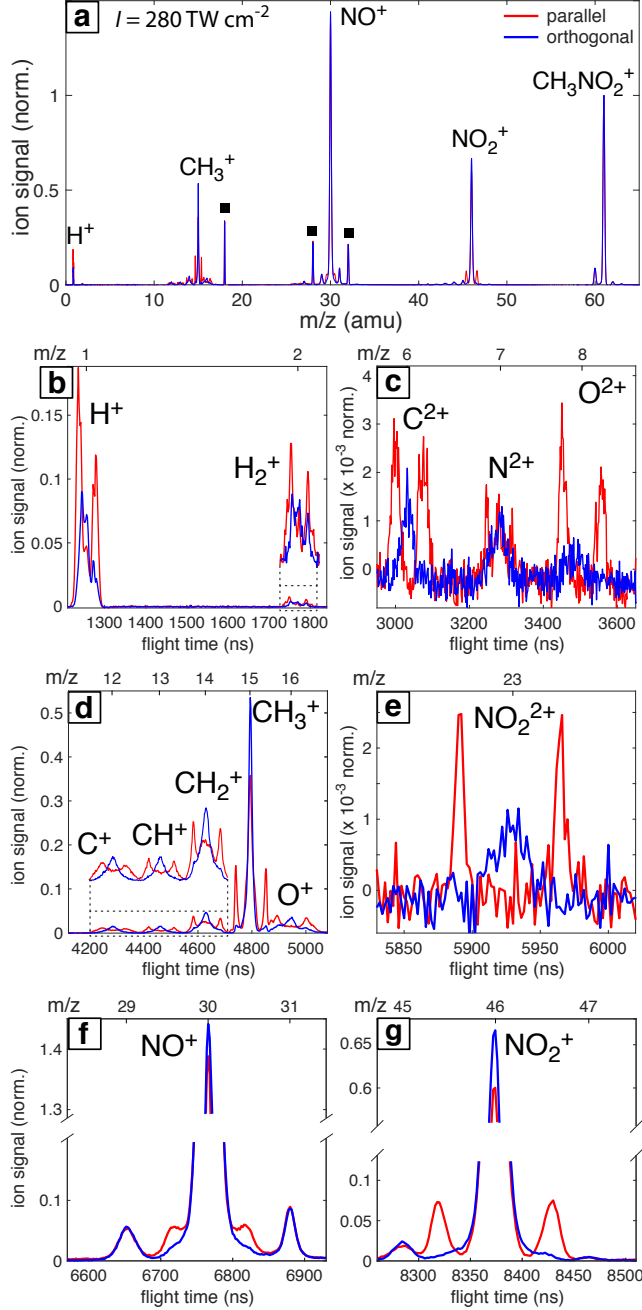


Figure 9: Mass spectra of NM (a) and magnified regions with split peaks resulting from Coulomb explosion (b–g). Peaks marked with a square come from air ( $\text{H}_2\text{O}^+$ ,  $\text{N}_2^+$ ,  $\text{O}_2^+$ ).

Figure 9a shows the mass spectra of NM taken with parallel (red) and orthogonal (blue) polarization at an intensity of  $280 \text{ TW cm}^{-2}$ . Panels b–g magnify selected flight time regions corresponding to the signals for  $\text{H}^+$  and  $\text{H}_2^+$  (b),  $\text{C}^{2+}$ ,  $\text{N}^{2+}$ , and  $\text{O}^{2+}$  (c),  $\text{CH}_n^+$  ( $n = 0-3$ ) and  $\text{O}^+$  (d),  $\text{NO}_2^{2+}$  (e),  $\text{NO}^+$  (f), and  $\text{NO}_2^+$  (g). All spectra taken with parallel laser polarization

exhibit split peaks surrounding the main  $m/z$  features that are either absent or significantly suppressed in the spectra taken with orthogonal polarization, indicating that dissociation occurs within one rotational period. The rotational constants for NM<sup>51</sup> of 0.44504, 0.35172, and 0.19599 cm<sup>-1</sup> correspond to 75, 95, and 170 ps periods. Hence, any metastable multiply charged ions formed in our experiments dissociate within  $\sim$ 100 ps. Moreover, the flight time separation between the left and right peaks in the ion signals does not change with increasing laser intensity (Supporting Information, Figure S2), which indicates that multiply charged NM ion fragments are ejected with specific momenta. The threshold laser intensities at which each Coulomb exploded fragment in Figure 9 is observed are given in the Supporting Information, Table S3.

The most intense Coulomb explosion peaks are seen in CH<sub>3</sub><sup>+</sup> (Figure 9d) and NO<sub>2</sub><sup>+</sup> (Figure 9g). These signals also have the lowest threshold intensity of 60 TW cm<sup>-2</sup>, which suggests that they arise from direct dissociation of the dication via the pathway



Coulomb explosion in the fragments H<sup>+</sup> (Figure 9b), CH<sub>2</sub><sup>+</sup> and O<sup>+</sup> (Figure 9d), and NO<sup>+</sup> (Figure 9f), which could arise from three-body explosive dissociation, appear first at higher intensities in the range of 75–90 TW cm<sup>-2</sup> (Table S3). Doubly charged fragments NO<sub>2</sub><sup>2+</sup> (Figure 9e), C<sup>2+</sup>, N<sup>2+</sup>, and O<sup>2+</sup> only appear at high intensities above 155 TW cm<sup>-2</sup> for NO<sub>2</sub><sup>2+</sup> and 190 TW cm<sup>-2</sup> for the remaining fragments. The observation of intact NO<sub>2</sub><sup>2+</sup> is notable because this species has only previously been detected from electron impact ionization of NO<sub>2</sub>,<sup>52</sup> no intact NO<sub>2</sub><sup>2+</sup> was observed in photoionization experiments of NO<sub>2</sub>.<sup>53</sup>

To assess the validity of direct C–N cleavage in the dication via eq 3, the momentum distributions of the Coulomb exploded CH<sub>3</sub><sup>+</sup> and NO<sub>2</sub><sup>+</sup> signals were computed. Momentum distributions may be obtained by transforming the flight time axis into the relative

momentum axis via the formula<sup>49</sup>

$$p = zeF(t - t_0), \tag{4}$$

where  $z$  is the charge of the fragment,  $e$  is the elementary charge,  $F$  is the electric field strength between the ion repeller and extraction plates,  $t$  is the flight time, and  $t_0$  is the flight time corresponding to the nominal  $m/z$  value. The corresponding kinetic energy distributions can be obtained by transforming the flight time axis to kinetic energy via the formula<sup>50</sup>

$$E_k = \frac{(zeF)^2}{2m} \left( \frac{t_2 - t_1}{2} \right)^2 \tag{5}$$

where  $m$  is the mass of the fragment, and  $t_1$  and  $t_2$  are the flight times of the left and right peaks, respectively. The total kinetic energy release from specific Coulomb explosion pathways can verify the computed decay energies.<sup>49</sup>

Figure 10 shows the momentum (a) and kinetic energy (b) distributions obtained at 280 TW cm<sup>-2</sup> for CH<sub>3</sub><sup>+</sup>, NO<sub>2</sub><sup>+</sup>, and NO<sub>2</sub><sup>2+</sup> for comparison. Due to low signal, the NO<sub>2</sub><sup>2+</sup> data are taken from the average of 2 × 10<sup>5</sup> laser shots, as compared to 10<sup>5</sup> shots for the other signals. All ion signals (dots) were fit to Gaussian distributions (solid lines) using least squares fitting. The corresponding momenta and kinetic energy distributions, with their FWHM extracted from the Gaussian fits are given in Table 2. It is evident from both Table 2 and Figure 10a that the momentum distributions of CH<sub>3</sub><sup>+</sup> (dark green) and NO<sub>2</sub><sup>+</sup> (blue) are the same, suggesting that they come from the same dissociation pathway (eq 3) as required by conservation of momentum. In contrast, NO<sub>2</sub><sup>2+</sup> (light blue) is ejected with significantly higher momentum. Based on the values in Table 2, the predicted total kinetic energy release of the pathway in eq 3 is 9.83 eV. This pathway assignment will be assessed computationally in Section 3.3.2 below. Momentum distributions for other Coulomb exploded fragments do not match the distributions of CH<sub>3</sub><sup>+</sup> and NO<sub>2</sub><sup>+</sup> or each other, so no additional pathways can be directly assigned. Both momentum and kinetic energy distributions of additional

fragments are given in the Supporting Information, Table S4.

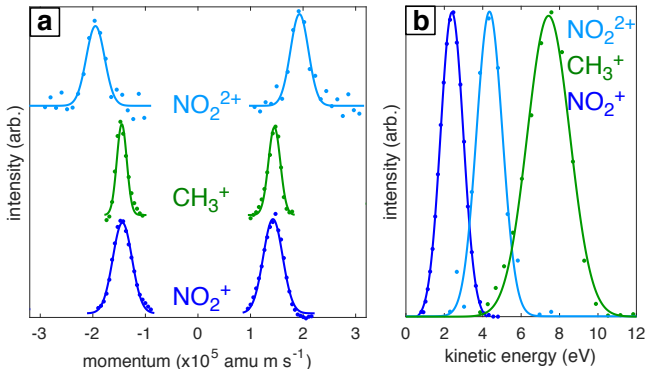


Figure 10: Momentum (a) and kinetic energy (b) distributions of Coulomb exploded fragments  $\text{NO}_2^+$ ,  $\text{CH}_3^+$ , and  $\text{NO}_2^{2+}$ .

Table 2: Extracted momentum and kinetic energy distributions from Coulomb explosion.

species	$\text{CH}_3^+$	$\text{NO}_2^+$	$\text{NO}_2^{2+}$
$p^a$	1.45	1.44	1.96
$\Delta p^b$	0.18	0.30	0.25
$E_k^c$	7.43	2.40	4.35
$\Delta E_k$	1.83	1.01	1.18

$a$ : units  $\times 10^5 \text{ amu m s}^{-1}$ .  $b$ : FWHM of Gaussian distributions.  $c$ : units eV.

### 3.3.2 Dissociation pathways in nitromethane dication

A total of 12 geometrically stable structures of the NM dication were found (Figure 11a), 10 of which are lower in energy than the structure with  $\text{CH}_3\text{-NO}_2$  topology (**XXXVI**, blue box). All geometrically stable structures are singlets; attempts to optimize geometries with triplet spin multiplicity resulted in dissociative formation of several charged fragments. Isomer **XXXVI** can rearrange into lower-energy isomers **XXXIII** and **XXXII** via the pathway shown in Figure 11b by overcoming a modest 0.97 eV transition state barrier.

The only direct dissociation pathway in the NM dication from isomer **XXXVI** was found to be cleavage of the C–N bond to produce  $\text{NO}_2^+$  and  $\text{CH}_3^+$  via eq 3. Computation of the relaxed potential energy curves along the C–N coordinate in the NM dication (Figure 12a) indicates that the dication is metastable with respect to C–N cleavage by only 0.3 eV, which

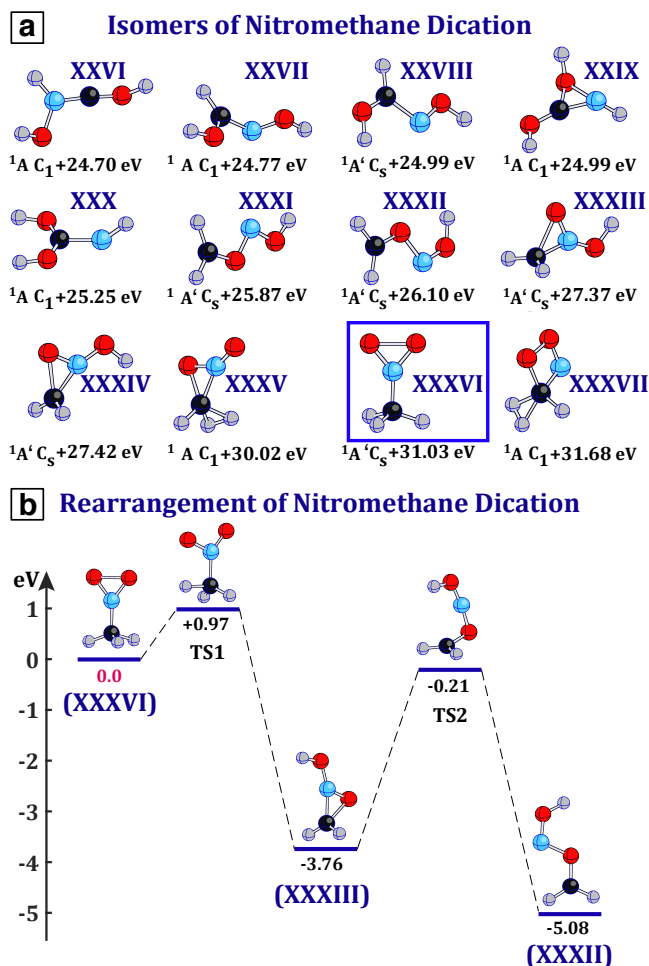


Figure 11: (a) The optimized states of the nitromethane dication with energies given with respect to the total energy of neutral NM. (b) Rearrangement pathway of nitromethane dication, with energies given with respect to that of isomer **XXXVI** at 0.0 eV.

is consistent with the intense correlated Coulomb explosion signals for  $\text{NO}_2^+$  and  $\text{CH}_3^+$  in Figure 9. The decay energy of this pathway was computed to be -9.06 eV relative to the NM dication, which matches with the total kinetic energy release of 9.83 eV from Table 2 to within the FWHM of the kinetic energy distributions, confirming that the Coulomb explosion signals arise from this dissociation pathway.

The dissociation pathway for proton abstraction to form  $\text{CH}_2\text{NO}_2^+$  (Figure 12b) was found to proceed from the rearranged NM dication structure **XXXIII**. The transition state leading to dissociation is lower than the initial rearrangement barrier of 0.97 eV relative to the parent NM dication structure (c.f., Figure 11b), indicating that dissociation is spontaneous.

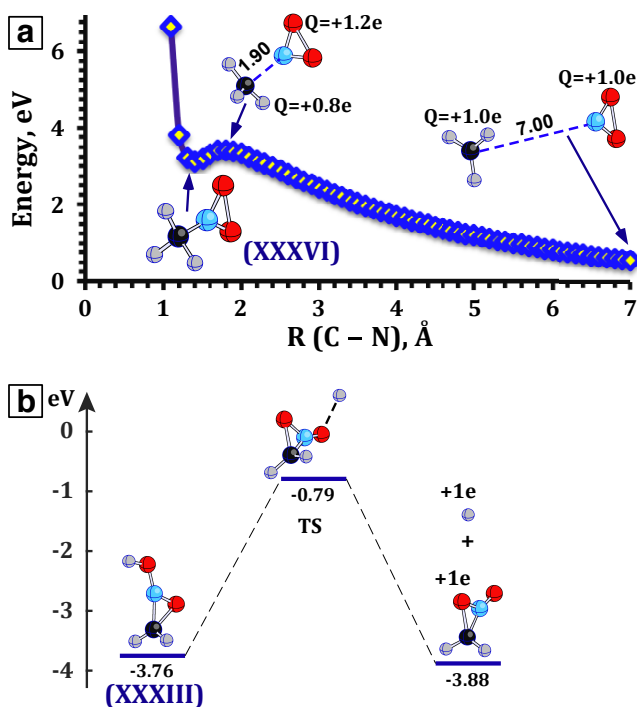


Figure 12: (a) Potential energy curve for C–N cleavage in the NM dication. Charges of the  $\text{CH}_3$  and  $\text{NO}_2$  units are shown at selected bond lengths. (b) Proton abstraction pathway from isomer **XXXIII** to produce  $\text{H}^+$  and  $\text{CH}_2\text{NO}_2^+$ . All energy shifts (in eV) are relative to the total energy of the nitromethane dication (31.03 eV with respect to neutral NM)

We expect that the proton loss pathway may contribute to the  $\text{CH}_2\text{NO}_2^+$  signal in our mass spectra due to the low energy requirement for dissociation from the dication as compared to neutral hydrogen abstraction from the singly charged cation (c.f., Figure 8). However, the associated rearrangement likely requires longer timescales than the rotational period of NM, and thus would not produce anisotropic Coulomb explosion signals in  $\text{H}^+$ . Hence, the  $\text{H}^+$  signal formed via this pathway in Figure 12b likely corresponds to the small central peak at  $m/z$  1 seen in Figure 9b. The Coulomb exploded  $\text{H}^+$  likely comes from the trication, as discussed below. We also found dissociation pathways of the rearranged dication leading to the ion pairs  $\text{NO}^+$  and  $\text{CH}_2\text{OH}^+$ ; and  $\text{CH}_2^+$  and  $\text{NO}_2\text{H}^+$  (Supporting Information, Figures S3 and S4). Since we do not see Coulomb explosion signals in the  $\text{CH}_2\text{OH}^+$  and  $\text{NO}_2\text{H}^+$  ions that would respectively be paired with  $\text{NO}^+$  and  $\text{CH}_2^+$ , it seems that the Coulomb explosion signals from  $\text{NO}^+$  and  $\text{CH}_2^+$  arise from the trication, as discussed in Section 3.3.3 below.

### 3.3.3 Dissociation pathways in nitromethane trication and higher charge states

The NM trication was found to be very fragile; despite the existence of five geometrically stable isomers (Supporting information, Figure S5), no rearrangements from the  $\text{CH}_3\text{-NO}_2$  topology could occur without fragmentation. The NM trication can undergo direct proton loss according to the relaxed potential energy curve shown in Figure 13a after overcoming a small barrier of 1.5 eV. Because very little Coulomb exploded  $\text{H}^+$  signal was observed at

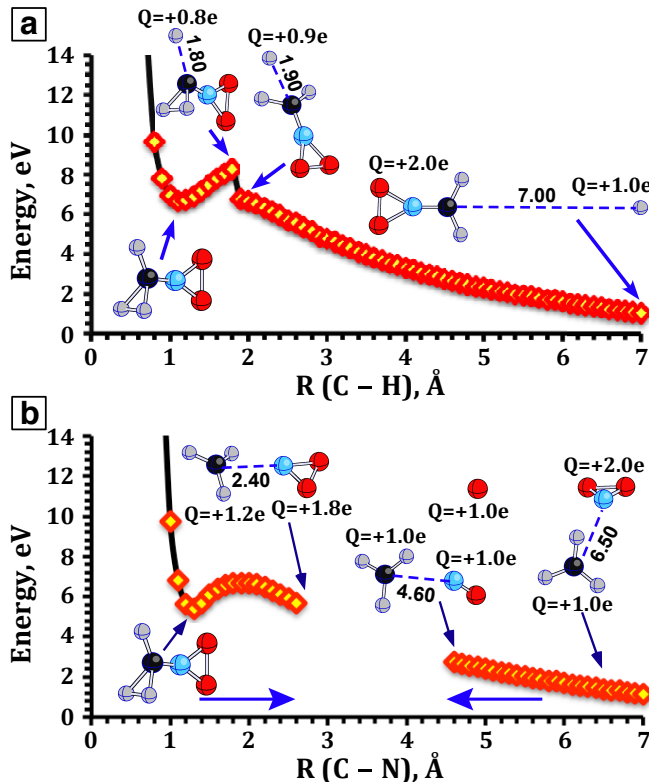


Figure 13: Dissociation of NM trication: relaxed potential energy curves for (a) proton loss, and (b) C–N bond cleavage. All energy shifts (in eV) are relative to the total energy of the nitromethane trication (57.47 eV with respect to neutral NM).

intensities below  $140 \text{ TW cm}^{-2}$  (Figure S2), we expect that much of the Coulomb exploded signal, unlike the central peak in Figure 9b discussed earlier, comes from direct dissociation of the trication either through this proton abstraction pathway or one of the explosion pathways discussed later in this section. We also note that the  $\text{CH}_2\text{NO}_2^{2+}$  ion has  $m/z$  30, matching that of  $\text{NO}^+$ . Hence, some of the Coulomb exploded signal assigned to  $\text{NO}^+$  in Figure 9f

could come from  $\text{CH}_2\text{NO}_2^{2+}$ . We also note that direct stretching or compression of one N–O bond in the trication can eject  $\text{O}^+$  or  $\text{O}_2^+$ , respectively (Figure S6).

To assess whether the observed  $\text{NO}_2^{2+}$  signal comes from direct dissociation of the NM trication, a relaxed potential energy scan along the C–N bond stretch in the trication was computed (Figure 13b). Spontaneous three-fragment dissociation was observed at  $R(\text{C–N}) > 2.6 \text{ \AA}$ . In an attempt to find a smooth dissociation curve, we started a new backward scan beginning with  $R(\text{C–N}) = 7.0 \text{ \AA}$ , but observed a similar spontaneous dissociation when  $R(\text{C–N}) < 4.6 \text{ \AA}$ . Hence, it is unlikely that intact  $\text{NO}_2^{2+}$  is formed by direct C–N cleavage in the trication. This instability at intermediate bond lengths likely results because the  $\text{NO}_2^{2+}$  itself is metastable with respect to  $\text{NO}^+ + \text{O}^+$  by 2 eV (Supporting Information, Figure S7).

To explain the formation of  $\text{NO}_2^{2+}$  and other Coulomb exploded fragments observed in Figure 9, we computed several explosions induced by bond stretches in the metastable trication state (Figure 14a–d) and ionization of the trication (Figure 14e–f). A trication state can explode either to three fragments with equal charges of  $+1e$  (Figure 14a–c) or to two fragments with one having charge  $+2e$  (Figure 14d). The three-body explosion pathways can account for the observed Coulomb explosion signals in  $\text{NO}^+$ ,  $\text{CH}_2^+$ , and  $\text{H}^+$ . Ionization of the trication results in spontaneous explosions with the formation of three fragments with charges of  $+1e$  or  $+2e$  (Figure 14e–f). Both of these pathways produce  $\text{NO}_2^{2+}$ , which suggests that this fragment arises from spontaneous explosion of quadruply ionized NM. These pathways also produce the observed fragments  $\text{CH}_2^+$ ,  $\text{CH}^+$ ,  $\text{H}_2^+$ , and  $\text{H}^+$ .

### 3.4 Discussion

The results of our mass spectral measurements and calculations both explain the findings of previous mass spectrometry studies on NM radical cation<sup>13–21</sup> and identify new dissociation pathways from higher cation charge states of NM. The contribution of both singly and multiply charged cations to shock detonation in energetic materials<sup>9,10</sup> makes the decomposition pathways identified in this work of potential importance to the energetic performance of NM.

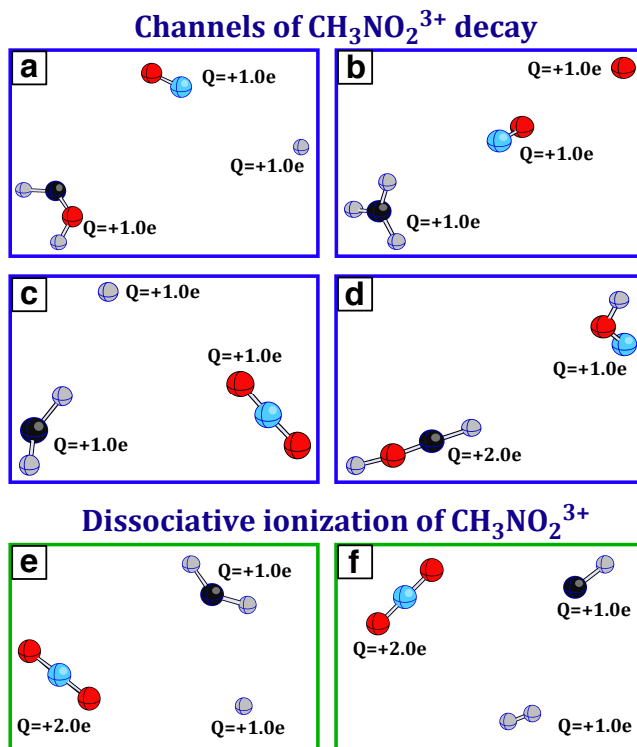


Figure 14: Explosions from the metastable NM trication induced by bond stretches (a–d) and ionization (e–f).

In particular, the rapid explosive decomposition pathways identified in NM dication and NM trication produce highly energetic charged fragments that could contribute to subsequent bimolecular reaction pathways in condensed-phase NM under detonation conditions.

In the singly charged cation, we identified rearrangement-dissociation pathways producing  $\text{NO}^+$ ,  $\text{CH}_2\text{OH}^+$ , and  $\text{CH}_2\text{NO}^+$  that have barriers of only 1.11 eV or lower. Of these fragments, only  $\text{NO}^+$  was observed in high yield in our mass spectra, consistent with previous strong-field fs laser ionization measurements.<sup>22–24</sup> The high yield of  $\text{NO}^+$  suggests that population of a particular excited state in NM cation by the laser pulse might induce selective fragmentation to  $\text{NO}^+$ . Selective fragmentation upon cationic excited state population has been observed in many molecules in fs laser mass spectrometry experiments.<sup>54–61</sup> Moreover, formation of  $\text{NO}^+$  from NM cation has been attributed to population of the second band in the photoelectron spectrum  $\sim 0.7$  eV above the first band.<sup>18</sup> This energy gap is below the 0.95 eV photon energy in our experiments, making population of this low-lying excited

state likely in our experiments. In contrast, the prevalence of the dissociation pathways to  $\text{CH}_2\text{OH}^+$  and  $\text{CH}_2\text{NO}^+$  upon collision-induced dissociation of NM cation<sup>19,21</sup> suggest that under high pressure conditions relevant to detonation, these dissociation pathways from the *aci*-nitromethane cation could play a larger role than in our experiments. The lack of  $\text{CH}_3^+$  formation at low laser intensity in our experiments can also be explained by the contributions of cationic excited states. The excess kinetic energy of  $\text{CH}_3^+$  and its higher appearance energy than  $\text{NO}_2^+$  observed in previous mass spectrometry studies<sup>13,14</sup> has been attributed to  $\text{CH}_3^+$  formation requiring population of the electronic excited state of  $\text{NM}^+$  corresponding to the third photoelectron band  $\sim 3$  eV above  $IE_{\text{vert}}$ .<sup>17</sup> At low intensity near the ionization threshold, negligible population of excited states in excess of the 0.95 eV photon energy above  $IE_{\text{vert}}$  is expected, which accounts for the lack of  $\text{CH}_3^+$  formation.

Rapid fragmentation of multiply charged NM cations was observed both through analysis of Coulomb explosion in the mass spectra and pathway computations. The dication was found to Coulomb explode into  $\text{NO}_2^+ + \text{CH}_3^+$ , with an experimental kinetic energy release of 9.83, matching the computed decay energy of -9.06 eV to within the FWHM of  $\sim 1$  eV in the measured distributions. The rapid explosion of the NM dication is expected because the difference in vertical and adiabatic  $IE$  values of 0.43 eV (31.46 eV and 31.03 eV, respectively, obtained from adding  $IE$  values in Table 1) exceeds the 0.3 eV barrier to dissociation computed in Figure 12a. This result is also consistent with the fact that no  $\text{CH}_3\text{NO}_2^{2+}$  was observed at  $m/z$  30.5 in the mass spectra at intensities near the threshold for Coulomb explosion in  $\text{NO}_2^+$  and  $\text{CH}_3^+$ . Additional Coulomb exploded fragments can be attributed to explosion from the metastable NM trication ( $\text{H}^+$ ,  $\text{CH}_2^+$ ,  $\text{NO}^+$ ) or instantaneous fragmentation from quadruply charged NM ( $\text{NO}_2^{2+}$ ,  $\text{CH}^+$ ,  $\text{H}_2^+$ ). The observed doubly charged atomic species  $\text{C}^{2+}$ ,  $\text{N}^{2+}$ , and  $\text{O}^{2+}$  must come from removal of more than four electrons from NM, indicating that high intensities of  $\sim 200$  TW  $\text{cm}^{-2}$  are sufficient to remove at least five electrons from NM. We note that further confirmation of all identified Coulomb explosion pathways could be obtained by coincident ion momentum imaging, as recently reported

for iodomethane.<sup>62</sup> Finally, we cannot rule out contributions from higher initial NM charge states than the computed trication to fragment ion signals at high laser intensity. It is likely that  $\sim 200 \text{ TW cm}^{-2}$  intensity exceeds the classical over-the-barrier ionization threshold<sup>63</sup> in NM, which would facilitate removal of multiple electrons and instantaneous nonspecific fragmentation into multiple products.

## 4 Conclusion

We have presented a systematic study of the dissociation pathways in singly and multiply charged NM cations through complementary femtosecond laser mass spectrometry measurements and high-level DFT computations. The NM cation was found to undergo both direct dissociation to  $\text{NO}_2^+$  or  $\text{CH}_3^+$  with low energy barriers and rearrangement to methylnitrite or *aci*-nitromethane isomers that produced  $\text{NO}^+$ ,  $\text{CH}_2\text{OH}^+$ , and  $\text{CH}_2\text{NO}^+$ . Our computations identified a total of 25 geometrically stable NM cation isomers, including some previously unreported isomers that play a role in dissociation pathways. Both the NM dication and trication were found to be metastable, and undergo Coulomb explosion to produce numerous charged fragments. The only Coulomb explosion pathway in the dication was found to form  $\text{CH}_3^+$  and  $\text{NO}_2^+$ , as verified by both momentum distributions from Coulomb explosion and the matching of the kinetic energy release distribution with the computed decay energy. Other Coulomb explosion pathways from the metastable trication and after loss of four electrons produced  $\text{NO}^+$ ,  $\text{CH}_2^+$ ,  $\text{H}^+$ ,  $\text{NO}_2^{2+}$ , and  $\text{H}_2^+$ . Collectively, our results reveal extensive fragmentation pathways in NM cations that produce highly energetic charged fragments. These pathways could be relevant to evaluating the energetic behavior of NM under shock detonation conditions where initial formation of highly charged cations and anions can play a role in the initiation of decomposition.

## Acknowledgement

Portions of this research were conducted with high-performance computational resources provided by the Louisiana Optical Network Initiative (<http://www.loni.org>). This research has also used resources of the National Energy Research Scientific Computing Center, a DOE Office of Science User Facility supported by the Office of Science of the U.S. Department of Energy under Contract No. DE-AC02-05CH11231. G.L.G. and K.M.T. acknowledge the support of the U.S. Army Research Office through Contract W911NF-19-1-0099. B.R.R. acknowledges the support from the National Science Foundation under Grant Number OIA-1541079. D.A.B. acknowledges generous financial support from an Altria Graduate Research Fellowship. The work has been performed in accordance with the Russian Government state task (State registration No. AAAA-A19-119092390076-7).

## Supporting Information Available

Tabulated decay energies, threshold intensities, and Coulomb explosion momentum/kinetic energy distributions; additional figures of molecular structures and dissociation pathways. This information is available free of charge via the Internet at <http://pubs.acs.org>.

## References

- (1) Taylor, W. D.; Allston, T. D.; Moscato, M. J.; Fazekas, G. B.; Kozlowski, R.; Takacs, G. A. Atmospheric Photodissociation Lifetimes for Nitromethane, Methyl Nitrite, and Methyl Nitrate. *Int. J. Chem. Kinet.* **1980**, *12*, 231–240.
- (2) Kelzenberg, S.; Eisenreich, N.; Eckl, W.; Weiser, V. Modelling Nitromethane Combustion. *Propellants Explos. Pyrotech.* **1999**, *24*, 189–194.

- (3) Winey, J. M.; Gupta, Y. M. Shock-Induced Chemical Changes in Neat Nitromethane: Use of Time-Resolved Raman Spectroscopy. *J. Phys. Chem. B* **1997**, *101*, 10733–10743.
- (4) Sikder, A.; Sikder, N. A Review of Advanced High Performance, Insensitive and Thermally Stable Energetic Materials Emerging for Military and Space Applications. *J. Hazard. Mater.* **2004**, *112*, 1 – 15.
- (5) Kaiser, R. I.; Maksyutenko, P. Novel Reaction Mechanisms Pathways in the Electron Induced Decomposition of Solid Nitromethane ( $\text{CH}_3\text{NO}_2$ ) and D3-Nitromethane ( $\text{CD}_3\text{NO}_2$ ). *J. Phys. Chem. C* **2015**, *119*, 14653–14668.
- (6) Woods, E.; Dessiaterik, Y.; Miller, R. E.; Baer, T. Dynamics in the Early Stages of Decomposition in Liquid Nitromethane and Nitromethane-Diethylamine Mixtures. *J. Phys. Chem. A* **2001**, *105*, 8273–8280.
- (7) Riad Manaa, M.; Reed, E. J.; Fried, L. E.; Galli, G.; Gygi, F. Early Chemistry in Hot and Dense Nitromethane: Molecular Dynamics Simulations. *J. Chem. Phys.* **2004**, *120*, 10146–10153.
- (8) Citroni, M.; Bini, R.; Pagliai, M.; Cardini, G.; Schettino, V. Nitromethane Decomposition under High Static Pressure. *J. Phys. Chem. B* **2010**, *114*, 9420–9428.
- (9) Reed, E. J. Electron-Ion Coupling in Shocked Energetic Materials. *J. Phys. Chem. C* **2012**, *116*, 2205–2211.
- (10) Pellouchoud, L. A.; Reed, E. J. Optical Characterization of Chemistry in Shocked Nitromethane with Time-Dependent Density Functional Theory. *J. Phys. Chem. A* **2013**, *117*, 12288–12298.
- (11) Nelson, T.; Bjorgaard, J.; Greenfield, M.; Bolme, C.; Brown, K.; McGrane, S.;

- Scharff, R. J.; Tretiak, S. Ultrafast Photodissociation Dynamics of Nitromethane. *J. Phys. Chem. A* **2016**, *120*, 519–526.
- (12) Dey, A.; Fernando, R.; Abeysekera, C.; Homayoon, Z.; Bowman, J. M.; Suits, A. G. Photodissociation Dynamics of Nitromethane and Methyl Nitrite by Infrared Multiphoton Dissociation Imaging with Quasiclassical Trajectory Calculations: Signatures of the Roaming Pathway. *J. Chem. Phys.* **2014**, *140*, 054305.
- (13) Kandel, R. J. Appearance Potential Studies. II. Nitromethane. *J. Chem. Phys.* **1955**, *23*, 84–87.
- (14) Niwa, Y.; Tajima, S.; Tsuchiya, T. Fragmentation of Energy-Selected Nitromethane Ions. *Int. J. Mass Spectrom. Ion Phys.* **1981**, *40*, 287 – 293.
- (15) Meyerson, S.; Fields, E. K. Mass Spectrum of Nitromethane. *Org. Mass Spectrom.* **1974**, *9*, 485–490.
- (16) Meisels, G. G.; Hsieh, T.; Gilman, J. P. Ion Fragmentation from Noninterconverting Electronic States. *J. Chem. Phys.* **1980**, *73*, 4126–4127.
- (17) Ogden, I.; Shaw, N.; Danby, C.; Powis, I. Completing Dissociation Channels of Nitromethane and Methyl Nitrite Ions and the Role of Electronic and Internal Modes of Excitation. *Int. J. Mass Spectrom. Ion Processes* **1983**, *54*, 41 – 53.
- (18) Gilman, J. P.; Hsieh, T.; Meisels, G. G. Competition Between Isomerization and Fragmentation of Gaseous Ions. II. Nitromethane and Methylnitrite Ions. *J. Chem. Phys.* **1983**, *78*, 1174–1179.
- (19) Egsgaard, H.; Carbea, L.; Elbel, S. Isomerizations of the Nitromethane Radical Cation in the Gas Phase. *Ber. Bunsenges. Phys. Chem.* **1986**, *90*, 369–374.
- (20) Egsgaard, H.; Carlsen, L.; Florêncio, H.; Drewello, T.; Schwarz, H. Aci-Nitromethane

- Generated and Characterized by Neutralization Reionization Mass Spectrometry. *Ber. Bunsenges. Phys. Chem.* **1989**, *93*, 76–80.
- (21) Lifshitz, C.; Rejwan, M.; Levin, I.; Peres, T. Unimolecular Fragmentations of the Nitromethane Cation. *Int. J. Mass Spectrom. Ion Processes* **1988**, *84*, 271 – 282.
- (22) Ledingham, K. W. D.; Deas, R. M.; Marshall, A.; McCanny, T.; Singhal, R. P.; Kilic, H. S.; Kosmidis, C.; Langley, A. J.; Shaikh, W. A Comparison of Femtosecond and Nanosecond Multiphoton Ionization and Dissociation for Some Nitro-Molecules. *Rapid Commun. Mass Spectrom.* **1995**, *9*, 1522–1527.
- (23) Kilic, H. S.; Ledingham, K. W. D.; Kosmidis, C.; McCanny, T.; Singhal, R. P.; Wang, S. L.; Smith, D. J.; Langley, A. J.; Shaikh, W. Multiphoton Ionization and Dissociation of Nitromethane Using Femtosecond Laser Pulses at 375 and 750 nm. *J. Phys. Chem. A* **1997**, *101*, 817–823.
- (24) Guo, Y. Q.; Bhattacharya, A.; Bernstein, E. R. Photodissociation Dynamics of Nitromethane at 226 and 271 nm at Both Nanosecond and Femtosecond Time Scales. *J. Phys. Chem. A* **2009**, *113*, 85–96.
- (25) Ferrier, B.; Boulanger, A.-M.; Holland, D. M.; Shaw, D. A.; Mayer, P. M. Nitro–Nitrite Isomerization and Transition State Switching in the Dissociation of Ionized Nitromethane: A Threshold Photoelectron–Photoion Coincidence Spectroscopy Study. *Eur. J. Mass Spectrom.* **2009**, *15*, 157–166.
- (26) McKee, M. L. Isomerization of the Nitromethane and Methyl Nitrite Radical Cations. A Theoretical Study. *J. Phys. Chem.* **1986**, *90*, 2335–2340.
- (27) Baer, T.; Hass, J. R. The Dissociation Mechanism of Methyl Nitrite Ions: Evidence for the Participation of Lower-Energy Isomeric Structures. *J. Phys. Chem.* **1986**, *90*, 451–455.

- (28) Türker, L.; Variş, S. Interaction of an  $\alpha$ -Particle with TATB. *Z. Anorg. Allg. Chem.* **2014**, *640*, 1727–1731.
- (29) Türker, L. Directional Interactions of  $\alpha$ -Particles with FOX-7. A DFT Study. *Propellants Explos. Pyrotech.* **2015**, *40*, 180–184.
- (30) Mullen, C.; Coggiola, M. J.; Oser, H. Femtosecond Laser Photoionization Time-of-Flight Mass Spectrometry of Nitro-Aromatic Explosives and Explosives Related Compounds. *J. Am. Soc. Mass Spectrom.* **2009**, *20*, 419–429.
- (31) Schröder, D. Coulomb Explosions and Stability of Multiply Charged Ions in the Gas Phase. *Angew. Chem. Int. Ed.* **2004**, *43*, 1329–1331.
- (32) Böhme, D. K. Multiply-charged Ions and Interstellar Chemistry. *Phys. Chem. Chem. Phys.* **2011**, *13*, 18253–18263.
- (33) Price, S. D.; Fletcher, J. D.; Gossan, F. E.; Parkes, M. A. Bimolecular Reactions of the Dications and Trications of Atoms and Small Molecules in the Gas-Phase. *Int. Rev. Phys. Chem.* **2017**, *36*, 145–183.
- (34) Maclot, S.; Piekarski, D. G.; Domaracka, A.; Méry, A.; Vizcaino, V.; Adoui, L.; Martín, F.; Alcamí, M.; Huber, B. A.; Rousseau, P.; et al., Dynamics of Glycine Dications in the Gas Phase: Ultrafast Intramolecular Hydrogen Migration versus Coulomb Repulsion. *J. Phys. Chem. Lett.* **2013**, *4*, 3903–3909.
- (35) Gutsev, G. L.; Ampadu Boateng, D.; Jena, P.; Tibbetts, K. M. A Theoretical and Mass Spectrometry Study of Dimethyl Methylphosphonate: New Isomers and Cation Decay Channels in an Intense Femtosecond Laser Field. *J. Phys. Chem. A* **2017**, *121*, 8414–8424.
- (36) Ampadu Boateng, D.; Gutsev, G. L.; Jena, P.; Tibbetts, K. M. Ultrafast Coherent

- Vibrational Dynamics in Dimethyl Methylphosphonate Radical Cation. *Phys. Chem. Chem. Phys.* **2018**, *20*, 4636–4640.
- (37) Ampadu Boateng, D.; Gutsev, G. L.; Jena, P.; Tibbetts, K. M. Dissociation Dynamics of 3- and 4-Nitrotoluene Radical Cations: Coherently Driven C–NO<sub>2</sub> Bond Homolysis. *J. Chem. Phys.* **2018**, *148*, 134305.
- (38) Ampadu Boateng, D.; Word, M. D.; Gutsev, L. G.; Jena, P.; Tibbetts, K. M. Conserved Vibrational Coherence in the Ultrafast Rearrangement of 2-Nitrotoluene Radical Cation. *J. Phys. Chem. A* **2019**, *123*, 1140–1152.
- (39) Gutsev, G. L.; López Peña, H. A.; McPherson, S. L.; Boateng, D. A.; Ramachandran, B. R.; Gutsev, L. G.; Tibbetts, K. M. From Neutral Aniline to Aniline Trication: A Computational and Experimental Study. *J. Phys. Chem. A* **2020**, *124*, 3120–3134.
- (40) Chai, J.-D.; Head-Gordon, M. Long-Range Corrected Hybrid Density Functionals with Damped Atom-Atom Dispersion Corrections. *Phys. Chem. Chem. Phys.* **2008**, *10*, 6615–6620.
- (41) Frisch, M.; Trucks, G.; Schlegel, H.; Scuseria, G.; Robb, M.; Cheeseman, J.; Scalmani, G.; Barone, V.; Mennucci, B.; Petersson, G.; et al, Gaussian 16 Rev. B.01. 2016.
- (42) Dunning, T. H. Gaussian Basis Sets for Use in Correlated Molecular Calculations. I. The Atoms Boron Through Neon and Hydrogen. *J. Chem. Phys.* **1989**, *90*, 1007–1023.
- (43) NIST Standard Reference Database Number 69. <http://webbook.nist.gov/chemistry/>, Last checked 7/17/20.
- (44) Maksić, Z. B.; Kovačević, B.; Vianello, R. Advances in Determining the Absolute Proton Affinities of Neutral Organic Molecules in the Gas Phase and Their Interpretation: A Theoretical Account. *Chem. Rev.* **2012**, *112*, 5240–5270.

- (45) Fukui, K. The Path of Chemical Reactions - The IRC Approach. *Acc. Chem. Res.* **1981**, *14*, 363–368.
- (46) Keldysh, L. Ionization in Field of a Strong Electromagnetic Wave. *Sov. Phys. JETP* **1965**, *20*, 1307–1314.
- (47) Yatsushashi, T.; Nakashima, N. Dissociation and Multiply Charged Silicon Ejection in High Abundance from Hexamethyldisilane. *J. Phys. Chem. A* **2010**, *114*, 11890–11895.
- (48) Yatsushashi, T.; Nakashima, N.; Azuma, J. Coulomb Explosion of Dichloroethene Geometric Isomers at 1 PW cm<sup>-2</sup>. *J. Phys. Chem. A* **2013**, *117*, 1393–1399.
- (49) Hoshina, K.; Hagihara, H.; Tsuge, M. Double Ionization and Coulomb Explosion of the Formic Acid Dimer by Intense Near-Infrared Femtosecond Laser Pulses. *J. Phys. Chem. A* **2012**, *116*, 826–831.
- (50) Yatsushashi, T.; Nakashima, N. Multiple Ionization and Coulomb Explosion of Molecules, Molecular Complexes, Clusters and Solid Surfaces. *J. Photochem. Photobiol. C* **2018**, *34*, 52 – 84.
- (51) NIST Computational Chemistry Comparison and Benchmark DataBase. <https://cccbdb.nist.gov/introx.asp>, (accessed April 2, 2020).
- (52) Stephan, K.; Helm, H.; Kim, Y. B.; Seykora, G.; Ramler, J.; Grössl, M.; Märk, E.; Märk, T. D. Single and Double Ionization of Nitrogen Dioxide by Electron Impact from Threshold up to 180 eV. *J. Chem. Phys.* **1980**, *73*, 303–308.
- (53) Masuoka, T.; Kobayashi, A. Single- and double-photoionization cross-sections of nitrogen dioxide (NO<sub>2</sub>) and ionic fragmentation of NO<sub>2</sub><sup>+</sup> and NO<sub>2</sub><sup>2+</sup>. *Chem. Phys.* **2004**, *302*, 31 – 41.

- (54) Itakura, R.; Watanabe, J.; Hishikawa, A.; Yamanouchi, K. Ionization and Fragmentation Dynamics of Benzene in Intense Laser Fields by Tandem Mass Spectroscopy. *J. Chem. Phys.* **2001**, *114*, 5598–5606.
- (55) Trushin, S. A.; Fuß, W.; Schmid, W. E. Dissociative Ionization at High Laser Intensities: Importance of Resonances and Relaxation for Fragmentation. *J. Phys. B: At. Opt. Mol. Phys.* **2004**, *37*, 3987–4011.
- (56) Yatsushashi, T.; Nakashima, N. Effects of Polarization of 1.4  $\mu\text{m}$  Femtosecond Laser Pulses on the Formation and Fragmentation of Naphthalene Molecular Ions Compared at the Same Effective Ionization Intensity. *J. Phys. Chem. A* **2005**, *109*, 9414–9418.
- (57) Wu, D.; Wang, Q.; Cheng, X.; Jin, M.; Li, X.; Hu, Z.; Ding, D. Effect of Cation Absorption on Ionization/Dissociation of Cycloketone Molecules in a Femtosecond Laser Field. *J. Phys. Chem. A* **2007**, *111*, 9494–9498.
- (58) Bohinski, T.; Tibbetts, K. M.; Tarazkar, M.; Romanov, D.; Matsika, S.; Levis, R. J. Measurement of an Electronic Resonance in a Ground-State, Gas-Phase Acetophenone Cation via Strong-Field Mass Spectrometry. *J. Phys. Chem. Lett.* **2013**, *4*, 1587–1591.
- (59) Bohinski, T.; Tibbetts, K. M.; Tarazkar, M.; Romanov, D.; Matsika, S.; Levis, R. Measurement of Ionic Resonances in Alkyl Phenyl Ketone Cations via Infrared Strong Field Mass Spectrometry. *J. Phys. Chem. A* **2013**, *117*, 12374–12381.
- (60) Bohinski, T.; Tibbetts, K. M.; Munkerup, K.; Tarazkar, M.; Romanov, D. A.; Matsika, S.; Levis, R. J. Radical cation Spectroscopy of Substituted Alkyl Phenyl Ketones via Tunnel Ionization. *Chem. Phys.* **2014**, *442*, 81 – 85.
- (61) Tibbetts, K. M.; Bohinski, T.; Munkerup, K.; Tarazkar, M.; Levis, R. Controlling Dissociation of Alkyl Phenyl Ketone Radical Cations in the Strong-Field Regime through Hydroxyl Substitution Position. *J. Phys. Chem. A* **2014**, *118*, 8170–8176.

- (62) Malakar, Y.; Pearson, W. L.; Zohrabi, M.; Kaderiya, B.; P., K. R.; Ziaee, F.; Xue, S.; Le, A. T.; Ben-Itzhak, I.; Rolles, D.; Rudenko, A. Time-resolved imaging of bound and dissociating nuclear wave packets in strong-field ionized iodomethane. *Phys. Chem. Chem. Phys.* **2019**, *21*, 14090–14102.
- (63) Ivanov, I. A.; Kheifets, A. S.; Calvert, J. E.; Goodall, S.; Wang, X.; Xu, H.; Palmer, A. J.; Kielpinski, D.; Litvinyuk, I. V.; Sang, R. T. Transverse Electron Momentum Distribution in Tunneling and Over the Barrier Ionization by Laser Pulses with Varying Ellipticity. *Sci. Rep.* **2016**, *6*, 19002.

# TOC Graphic

